On the Formation of Stray Grains in Directionally-Solidified Ni-Based Superalloys with Varying Cross Sections

H. Ebrahimiyan[1], A. Kermanpur[1, *], A. R. Heydari[1], D. Heydari[2] and M. Bahmani[2]

* *ahmad_k@cc.iut.ac.ir*

Received: April 2017 Accepted: November 2017

[1] Department of Materials Engineering, Isfahan University of Technology, Isfahan, Iran.
[2] MAPNA Turbine Blade Engineering & Manufacturing Co. PARTO, Karaj, Iran.

DOI: 10.22068/ijmse.14.4.12

Abstract: *Formation of stray grain defects particularly around re-entrant features of the turbine blade airfoils is one of the major problems in directional and single crystal solidification processes. In this work, directional solidification tests of the GTD-111 Ni-based superalloy were conducted at different withdrawal velocities of 3, 6 and 9 mm.min^{-1} using various stepped cylindrical and cubic designs. The process was also simulated using ProCAST finite element solver to characterize the crystal orientations. The phase transformation temperatures of the superalloy were estimated by the differential scanning calorimetry test. A process map was developed to predict the formation of stray grains in the platform regions of the stepped cylindrical and cubic specimens using the experimentally-validated simulation model. The process map shows critical values of the platform size, withdrawal velocity and initial sample size for the stray grain formation. The withdrawal velocity, platform size and initial sample size all had an inverse effect on the formation of stray grains.*

Keywords: *Directional Solidification, Ni-Based Superalloy, Computer Simulations, Stray Grain, Process Map.*

1. INTRODUCTION

Directionally solidified (DS) and single crystal (SC) Ni-based turbine blades have been introduced for further improvement of performance in aero-engines and industrial gas turbines. The solidification conditions of the DS/SC turbine blades must be well controlled to avoid the formation of deleterious casting defects. Thermal gradient ahead of the advancing solid/liquid interface plays a crucial role on the refinement of microstructures and the formation of different casting defects such as stray grains and freckles [1]. One of the major problems during production of the DS and SC turbine blades is the formation of stray grain defects particularly around re-entrant features (such as the platforms or shroud regions) of the turbine blade airfoils. Since stray grains are randomly orientated in the microstructure and have high-angle grain boundaries, they would decrease mechanical properties [1, 2]. While nucleation of a new grain in front of solid/liquid interface during SC solidification would lead to the formation of a stray grain, Reed [1] and Zhou [2] pointed out that for the DS blades, stray grains may be defined as those grains with orientation more than about 10 from <001> direction.

The behaviour of dendritic growth and the formation of stray grains in gas turbine blades is studied by several investigators. Imwinkelried et al. [3] suggested an analytical model for the prediction of stray grain formation in the platform ends based on the relation among the temperature difference, dendrite tip undercooling, and growth parameters. This model was then developed by Bussac and Gandin [4] to describe the condition of stray grain formation in a space where the thermal gradient and the withdrawal velocity of a Bridgman furnace apparatus are the controlling parameters. The limits of this process window were then refined in order to determine the influence of other parameters such as the crystallographic orientation of the single dendritic grain, the size of the platform in which the single grain has to extend, the growth kinetics of the dendrite tips, or the existence of a lateral thermal gradient. Gu et al. [5] modelled the movement and remelting of dendrite fragments originating in channels inside

the mush and studied the effects of remelting of the broken dendrite tips on stray grain formation. Such channels exist because of thermosolutal convective instabilities during solidification and persist as freckle chains in the solidified material. Only a small window of initial conditions existed which led to stray grain formation. This window corresponded to medium-sized fragments originating near the mouth of the channel. An experimental study, together with a two-dimensional numerical simulation of solute segregation, was conducted by D'Souza et al. [6] to investigate the mechanism for stray grain nucleation following seed melt-back and initial withdrawal. It was proposed that the factors contributing to stray grain nucleation during initial withdrawal are (1) the magnitude of local, solute-adjusted undercooling and (2) the rapidly changing curvature of the solidification front close to the mould walls during the initial solidification transient. The morphological constraints arising from the inclination of the primary dendrites from the seed crystal with respect to the mould wall determines the probability of the stray grain nuclei developing into equiaxed/columnar grains following competitive growth. Ma and Buhrig-Polaczek [7] proposed a heat conductor technique to reduce stray grain formation in a simplified geometry featuring a shroud-like cross-section using thermal numerical simulation.

Graphite is recommended as heat conductor material because of its excellent thermophysical properties. Both the extent and the period of undercooling at the platform extremity significantly decreased. Xuan et al. [8] showed that the formation of stray grains is due to the critical nucleus forming in the region of the cross section if the undercooling is more than a certain value at higher withdrawal velocities. Zhou [2] believed that diverging boundaries are the most favourable location for stray grain formation by bending or detachment of side arms during extension of secondary arms and the development of tertiary branches at the diverging boundaries. Yang et al. [9] reported that the factor contributing to the competitive growth is the rotation angle of the unfavourably oriented grain during the DS process of a bi-crystal. Meng et al. [10] showed that the stray grains tend to nucleate either in the inner corners of the platform or at a faster withdrawal velocity, which is associated with the corresponding thermal condition. Recently, a method for inhibiting the stray grain formation is proposed by Meng et al. [11] based on which assistant bars are designed to introduce the primary grain into these platforms according to the theory of seeding method. By this method, the primary grain is introduced to the large dimensional platforms by developing secondary and tertiary dendrites, inhibiting stray grains to form in the large dimensional platforms.

Although the above previous works show that great attentions have been paid upon the formation mechanisms of the stray grain defect during DS and SC solidification processes, there is still a lack of quantitative information on the relationship between the influencing process parameters and the occurrence of this important defect for the complex-shaped turbine blades with varying cross sections. The aim of the present work is to evaluate effects of platform size, sample shape and diameter and withdrawal velocity on the stray grain formation in the DS GTD-111 Ni-based superalloy, as one of the most important DS alloys frequently used in modern gas turbines. A process map showing the occurrence condition of stray grain formation as a function of platform size, withdrawal velocity and sample size is introduced using a computer simulation model verified with experimental measurements.

2. MATERIALS AND METHODS

2. 1. DS Experiments

The alloy used in the present study was the GTD-111 Ni-based superalloy whose chemical composition was determined by X-ray fluorescence and optical emission spectroscopy techniques (Table 1). Several stepped specimens of 150 mm length with two different platform regions were directionally solidified in a home-made Bridgman-type vacuum induction melting furnace. The schematic illustrations of the stepped cylindrical and cubic samples used for directional solidification are shown in Fig. 1. In

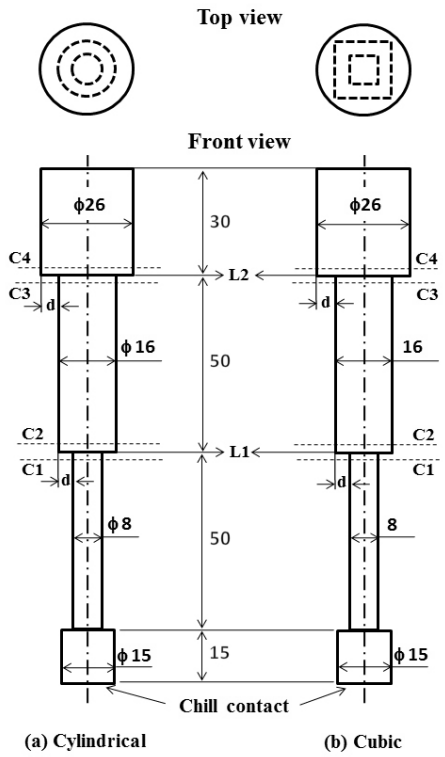

Fig. 1. Scheme of the stepped cylindrical and cubic specimens. The platform size is denoted by d (dimensions are in mm).

this figure the location of transverse cross sections C1, C2, C3 and C4 and the platform regions L1 and L2 are shown. Note that the initial diameter of the cylindrical sample and the side size of the cubic sample (D) are different for the platforms L1 and L2.

Several DS tests were conducted at different withdrawal velocities (R) of 3, 6 and 9 mm.min^{-1} using samples with different D values from 8 mm to 20 mm. At each DS test, a polycrystalline cylindrical rod of GTD-111 superalloy was re-melted in the ceramic mould under the reduced pressure of about 10^{-3} mbar, superheated to the temperature of about 1500 °C, held for about 10 min for temperature equalization, and finally withdrawn out of the heating zone based on the prescribed velocity using a withdrawal mechanism. The melt temperature was recorded during the withdrawal using an infrared pyrometer.

Differential scanning calorimetry (DSC) test was employed to determine the phase transformation temperatures including liquidus and solidus of the alloy, with the cooling rate of 5°C.min^{-1} in Helium atmosphere. Fig. 2 shows the DSC curve of the superalloy used in this

Table 1. Nominal chemical composition (wt%) of DS GTD-111 superalloy.

Element	Cr	Co	Al	Ti	W	Mo	Ta	Cu	S	P	Ni
Wt%	13.5	9.41	3.4	4.88	3.69	1.68	3.9	0.012	0.001	0.003	Bal.

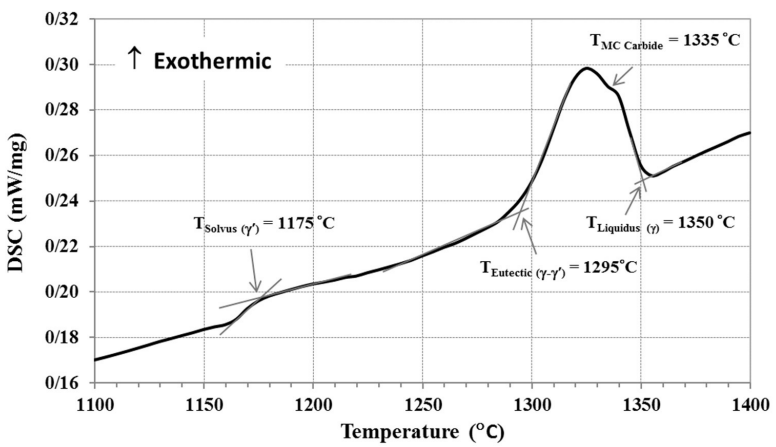

Fig. 2. DSC curve of the GTD-111 Ni-based superalloy under heating rate of 5 °C min^{-1}.

work. Different critical temperatures including γ'-solvus, γ/γ'-eutectic, MC carbide, and γ-liquidus temperatures were collected form the DSC curve as shown in Fig. 2. These critical temperatures corresponded well with the results in many other studies on the solidification of Ni-based superalloys [12, 13]. These temperatures were used in the simulation model, which is explained in the next section. The grain and dendritic structures in longitudinal and transverse directions of all as-cast specimens was characterized using an optical microscope equipped with camera. The grain structure was revealed by an etchant comprised of 25 g $FeCl_3$, 27 ml HCl (32%) and 40 ml H_2O. The macro-etchant for detection of the SGs contained 80 ml HCl, 2 ml HNO_3, 11 ml H_2O and 16 gr $FeCl_3$ and the micro-etchant was made by 33 ml CH_3COOH, 33 ml HNO_3, 33 ml H_2O and 1 ml HF.

2. 2. Grain Structure Simulation

Using the finite element ProCAST simulation software [14], a coupled thermal-structural model was developed to predict the formation of grain structure in the DS specimens using stepped cylindrical and cubic moulds. In this model, the heat transfer calculation was conducted in the macro-scale using the finite element method, while the grain structure with special consideration of the crystallographic anisotropy of grains and the growth kinetics of dendrite tips was predicted by a cellular automaton technique coupled with the finite element heat flow calculations [15]. During simulation, temperature at each time step is obtained from the heat-flow computation in a macro-scale finite element model. When the temperature becomes lower than the liquidus temperature, solidification starts by two mechanisms: heterogeneous nucleation and solid growth. To describe the heterogeneous nucleation, the continuous Gaussian nucleation distribution was used to relate the increase of grain density with undercooling [16],

$$n(\Delta T) = \frac{N_{max}}{\Delta T_\sigma \sqrt{2\pi}} \int_0^{\Delta T} \exp\left[-\left(\frac{\Delta T - \Delta T_m}{\Delta T_\sigma \sqrt{2}}\right)^2\right] d(\Delta T) \qquad (1)$$

where $n(\Delta T)$ is the total number of nuclei in the bulk liquid at the undercooling ΔT, ΔT_m is the mean nucleation undercooling, ΔT_σ is the standard deviation of the distribution and N_{max} is the maximum nuclei density. The increase of the undercooling of liquid metal affects the quantity of grains. The adjustable nucleation parameters which are associated with this distribution can be deduced from a few DTA type experiments [16]. In the present work, the required coefficients (ΔT_{max}, ΔT_σ and Nmax) were determined based on comparisons between the experimental micrographs and numerical simulations performed using different values of nucleation coefficients. The comparisons were made on the (1) surface grain structure and (2) stray grains formed in the specimens. Two different surface nucleation functions (unit of m^{-2}) were assigned for the chill/melt and ceramic mould/melt interfaces, while a volume nucleation function (unit of m^{-3}) was considered for the bulk of melt. The quantity of grains and their shape determined in the numerical simulation depend on the value of these characteristic coefficients (equation 1).

Table 2. Nucleation parameters used in the grain structure simulation runs.

Variable	ΔT_m (℃)	ΔT_σ (℃)	N_{max}
Surface nucleation (chill-plate)	2	1	1×10^8 (m^{-2})
Surface nucleation (mould wall)	6	1	1×10^4 (m^{-2})
Bulk nucleation	10	1	1×10^8 (m^{-3})

The optimum values are listed in Table 2. It was found that the maximum nuclei density had the largest influence on the results of the numerical simulation performed for the directional solidification process, as already shown by Szeliga et al. [17].

The continuous grain growth during the solidification process is caused by the undercooling of liquid metal. Neglecting the kinetic and curvature undercooling terms, the solid growth rate V can be calculated using KGT model [18]. Based on this model, the dendrite tip radius (R) and velocity (V) are determined by the two relationships:

$$\Omega=\frac{C^*-C_0}{C^*(1-k)}=\mathrm{Iv(Pe)} \quad (2)$$

and

$$\mathrm{R}=2\pi\sqrt{\left(\frac{\Gamma}{mG_C\xi_C-G}\right)} \quad (3)$$

where the solutal Peclet number, Pe, is given by:

$$\mathrm{Pe}=\frac{RV}{2D} \quad (4)$$

Ω is the supersaturation, c_0 is the initial concentration of the alloy, c^* is the concentration in the liquid at the tip, k is the partition coefficient, m is the liquidus slope, D is the diffusion coefficient in the liquid, Γ is the Gibbs-Thomson coefficient, and G_C is the solute gradient in the liquid at the tip. IN the dendritic regime, the thermal gradient (G) can be neglected. Iv(Pe) is the Ivantsov function of the Peclet number and ζ_C is also a function of the Peclet number which is close to unity at low growth rate. The undercooling (ΔT) is related to the supersaturation by the relationship:

$$\Delta T=mc_0\left[1-\frac{1}{1-\Omega\,(1-k)}\right] \quad (5)$$

Therefore, the relationship between the growth rate of the dendrite tip (V) and its undercooling (ΔT) is given by the solution of equations (2-5). In order to speed up the computations, the calculated velocity-undercooling data is fitted in a third order polynomial function as below:

$$V(\Delta T)=\mathrm{a_0}+\mathrm{a_1}\Delta T+\mathrm{a_2}\Delta T^2+\mathrm{a_3}\Delta T^3 \quad (6)$$

where a_0, a_1, a_2 and a_3 are constants. The equation (6) is implemented in the cellular-automaton finite element module of the ProCAST software to calculate growth kinetics of the dendrite tips.

In the present work, the growth kinetics of the superalloy GTD-111 was analysed using the multicomponent extension of the KGT model as suggested by Bobadilla et al. [19]. In this approach, the equivalent liquid concentration ($\bar{c}$), liquidus slope ($\bar{m}$), and partition coefficient ($\bar{k}$) are determined based on the chemical composition of the multicomponent alloy and the binary phase diagrams X-Y (X is the main alloying element and Y is the component of the superalloy) via the following relationships:

$$\bar{c}=\sum_{i=1}^{n}c_i \quad (7)$$

$$\bar{m}=\frac{\sum_{i=1}^{n}(m_i\cdot c_i)}{\bar{c}} \quad (8)$$

$$\bar{k}=\frac{\sum_{i=1}^{n}(m_i\cdot c_i\cdot k_i)}{\sum_{i=1}^{n}(m_i\cdot c_i)} \quad (9)$$

where c_i is the liquid concentration, m_i the liquidus slope, and k_i the partition coefficient for element i. The binary phase diagram data used in the present calculations are presented in Table 3 [20]. Table 4 shows the calculated values of the constants of the growth kinetics equation (6) which used in all simulation runs. The thermo-physical properties of the superalloy GTD-111, ceramic mould and copper chill, which are needed for the FE heat flow calculations, are shown in Table 5 [14].

Table 3. The value of distribution coefficient and the liquidus slope for the GTD-111 nickel superalloy [20].

Binary alloy system	Concentration c_i (wt%)	Distribution coefficient k_i	Liquidus slope m_i (K·(wt%)$^{-1}$)
Ni-Cr	13.5	0.6	-1.9
Ni-Co	9.41	1	-0.4
Ni-Mo	1.68	1	-0.001
Ni-Ta	3.9	0.25	-2
Ni-W	3.69	1	-2.4
Ni-Al	3.4	0.6	-4
Ni-Ti	4.88	0.5	-11.5

Table 4. Coefficients of the growth rate equation (6).

Constant	Value
a_0, a_1	0
a_2	7.494×10^{-7} (m·s^{-1}·K^{-2})
a_3	2.043×10^{-6} (m·s^{-1}·K^{-3})

Table 5. Thermal properties for GTD-111 superalloy, ceramic mould and copper chill.

Property	Value		
	Superalloy	Ceramic Mould	Copper Chill
Density (kg·m^{-3})	7530	2240	8165
Specific heat (kJ·kg^{-1}·K^{-1})	f(T)	1.207	0.49
Thermal conductivity (W·m^{-1}·K^{-1})	28	1.5	398
Solidus temperature (℃)	1295	---	---
Liquidus temperature (℃)	1350	---	---

3. RESULTS AND DISCUSSION

3. 1. Formation of Grain Structure

The experimental surface grain structures of the cylindrical and cubic specimens directionally-solidified at different withdrawal velocities are shown in Fig. 3. The solidification is started in the starter block from the chill surface at the bottom and is continued upwardly through the entire specimens. A columnar grain structure can be observed along the longitudinal axis for all specimens. The simulated surface longitudinal and transverse grain structures in cylindrical and cubic specimens directionally solidified under growth velocity of 6 mm.min^{-1} are shown in Figs. 4a and 4b, respectively, which is reasonably in agreement with the experimental

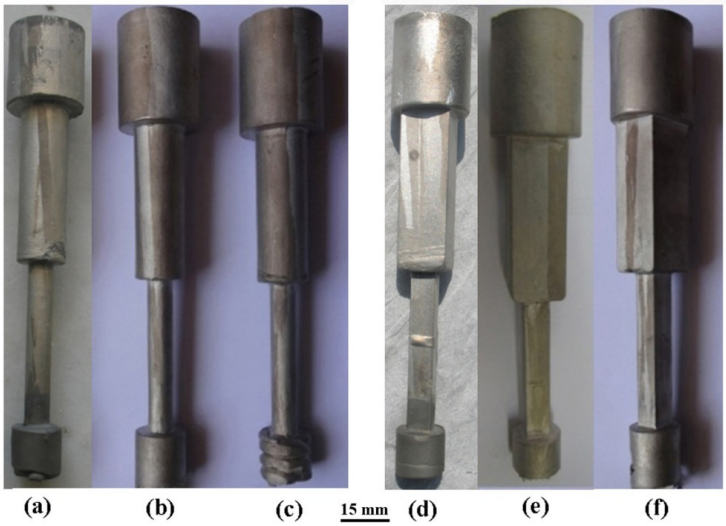

Fig. 3. The experimental surface grain structures of the (a, b, c) cylindrical and (d, e, f) cubic specimens grown at withdrawal velocity of (a, d) 3, (b, e) 6, and (c, f) 9 mm.min^{-1}.

observations. Due to the competitive grain growth mechanism, the number of grains (NG) is decreased during solidification. It is well known that Ni-based superalloys have a cubic crystal structure and the dendrite arms show regular cruciform when the <001> orientation is parallel to the direction of heat flow. Based on the experimentally observed four-fold symmetry of dendrite side-branches, it is generally believed that side-branching occurs along the <001> crystallographic direction [2]. Chalmers [21] explained the <001> growth direction of metal dendrites in terms of the region of dendrite tip being bound by the slowest-growing close-packed {111} planes. Ding and Tewari have reported that the microstructures of directionally solidified single crystals change along different crystallographic orientations, and that the side-branches in FCC metal alloys grew along the <001> crystallographic directions regardless of the direction of heat extraction [22]. Therefore, as shown in Figures 4a and 4b, it can be noticed that those grains whose the preferred crystallographic direction (e.g. <001> in cubic systems) are aligned parallel to the heat transfer direction will grow at the expense of the others. Table 6 shows the simulated NG values at different transverse cross sections of the cylindrical and cubic specimens at different growth velocities. It can be seen that, firstly, the NG value is decreased along the longitudinal direction for all conditions;

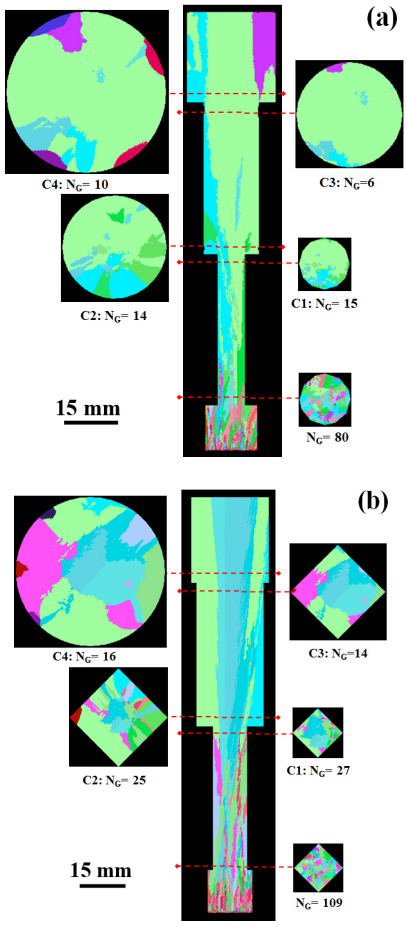

Fig. 4. The simulated surface longitudinal and transverse grain structures of the (a) cylindrical and (b) cubic specimens grown at withdrawal velocity of 6 mm.min^{-1}.

Table 6. The simulation results of the number of grains at different transverse cross sections (according to Fig.1) of cylindrical and cubic specimens grown under different withdrawal velocities.

Transverse cross section	Cylindrical specimen			Cubic specimen		
	3 mm.min^{-1}	6 mm.min^{-1}	9 mm.min^{-1}	3 mm.min^{-1}	6 mm.min^{-1}	9 mm.min^{-1}
C1	12	15	8	12	27	17
C2	12	14	7	10	25	20
C3	9	9	6	7	14	12
C4	10	10	11	7	16	14

Secondly, at a given withdrawal velocity, NG is higher in the cubic specimen compared to the cylindrical one, which is due to the higher external heat transfer surfaces of the cubic specimen. Thirdly, increasing the withdrawal velocity resulted in a higher NG; nevertheless, the lower NG for the withdrawal velocity of 9 mm.min^{-1} reveals that the decrement influence of the competitive grain growth mechanism is enhanced with increasing withdrawal velocity, resulting in a lower NG. Fourthly, the NG is increased when the solidification front is passed through the L2 platform. This shows that some strain grains should be formed at this platform.

3. 2. Formation of Stray Grains

Figures 5 and 6 show the experimental and simulated grain structures in the C2 and C4 transverse cross sections for different withdrawal velocities of 3, 6 and 9 mm.min^{-1}. These cross sections are selectively etched to identify only the stray grains. In the simulated grain structures, only grains whose misorientation is more than 15° are shown. These grains are considered as stray grains for all conditions. A good agreement can be seen between the experimental and simulation results of stray grain numbers as shown in Table 7. The results show that no stray

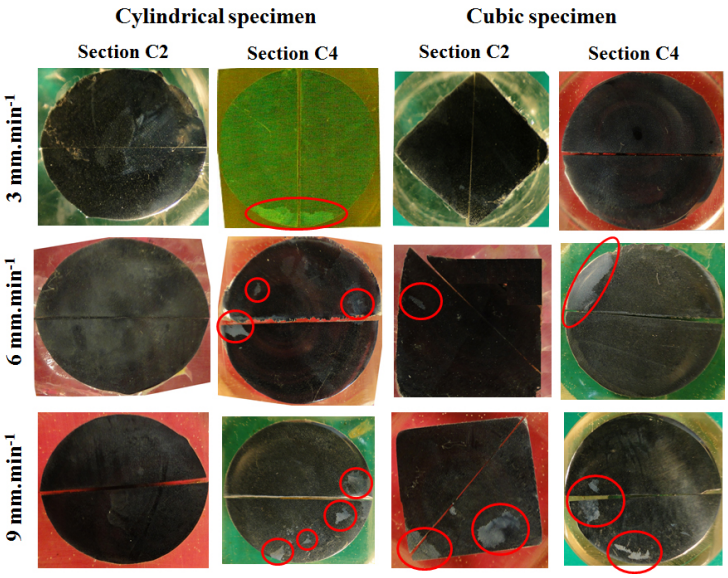

Fig. 5. The experimental transverse cross sections of the cylindrical and cubic specimens at different cross sections (C2 and C4) and withdrawal rates of 3, 6 and 9 mm.min^{-1}. Note that only stray grains are characterized in the cross sections with red circles. (Figures not to-scale)

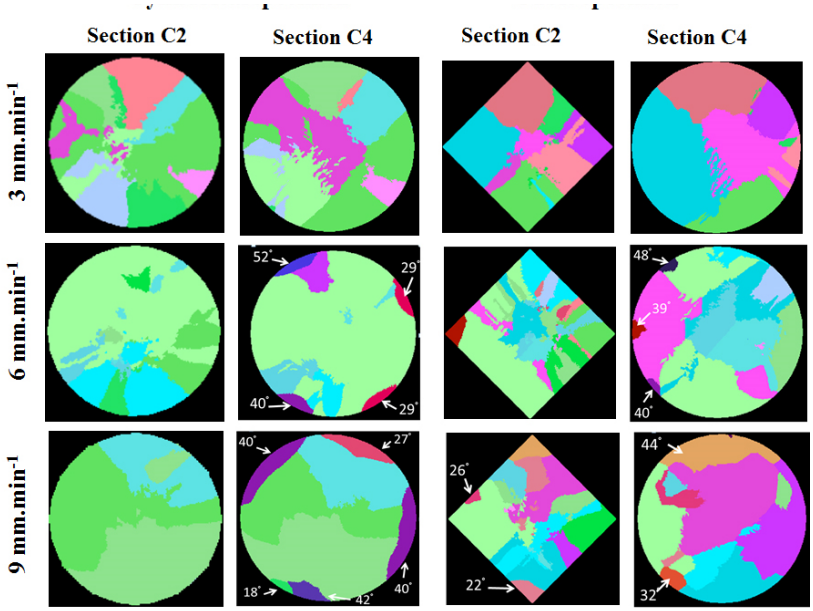

Fig. 6. The simulated transverse cross sections of the cylindrical and cubic specimens at different cross sections (C2 and C4) and withdrawal rates of 3, 6 and 9 mm.min^{-1}. Note that only stray grains with their deviation angle respect to the <100> crystallographic direction are shown. (Figures not to-scale)

grain is formed in the platform L1 of the cylindrical specimen for different withdrawal velocities; however, the number of stray grains is increased with increasing the withdrawal velocity in the platform L2 of both specimens. Some stray grains nucleated in the L1 platform might stop growing, while other might form in the L2 platform. This situation is shown in Fig. 7 for the cubic specimen directionally solidified under the withdrawal velocity of 9 mm.min^{-1}. It is seen that two stray grains formed in the platform L1 (with the misorientation of 22° and 26°) are stopped, while two new grains are nucleated in the platform L2 (with the misorientation of 32° and 44°). One should note that the platform size (d) and the initial sample diameter (D) are both different for these platforms.

In order to evaluate the condition of stray grain formation, thermal fields around the platform regions of the specimens were studied in details. As an example, Fig. 8 shows the evolution of thermal field in the longitudinal cross section of the cylindrical specimen directionally solidified at 6 mm.min^{-1}, when mushy zone is passing through the platforms L1 and L2. It can be seen that curvature of the mushy zone is remained convex when passing the L1 platform, while it is

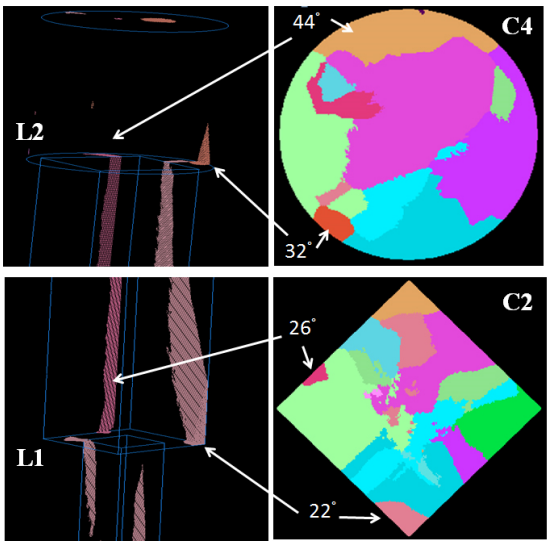

Fig. 7. The simulation results for the formation of stray grains in the L1 and L2 platforms of the cubic specimen grown at withdrawal velocity of 9 mm.min^{-1} and the resultant grain structures at the transverse cross sections of C2 and C4. (Figures not to-scale)

changed to concave in the corner of the platform L2. This is accompanied with a decrease in temperature gradient and therefore the cooling rate in these regions, as shown in Figs. 9(a) and

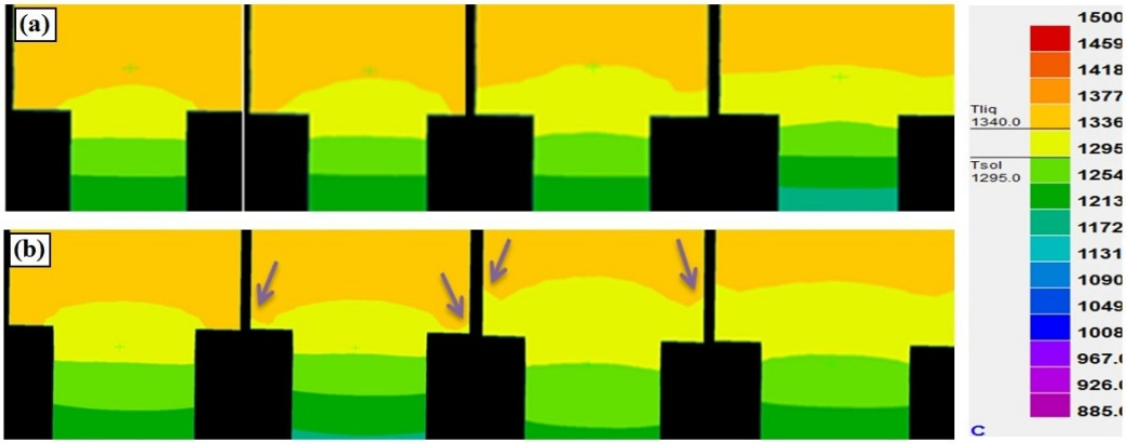

Fig. 8. The evolution of thermal field near the platforms (a) L1 and (b) L2 of the cylindrical specimen grown at 6 mm.min^{-1}. Time is increasing from left to right. The concave curvature of the isotherms is shown by arrow.

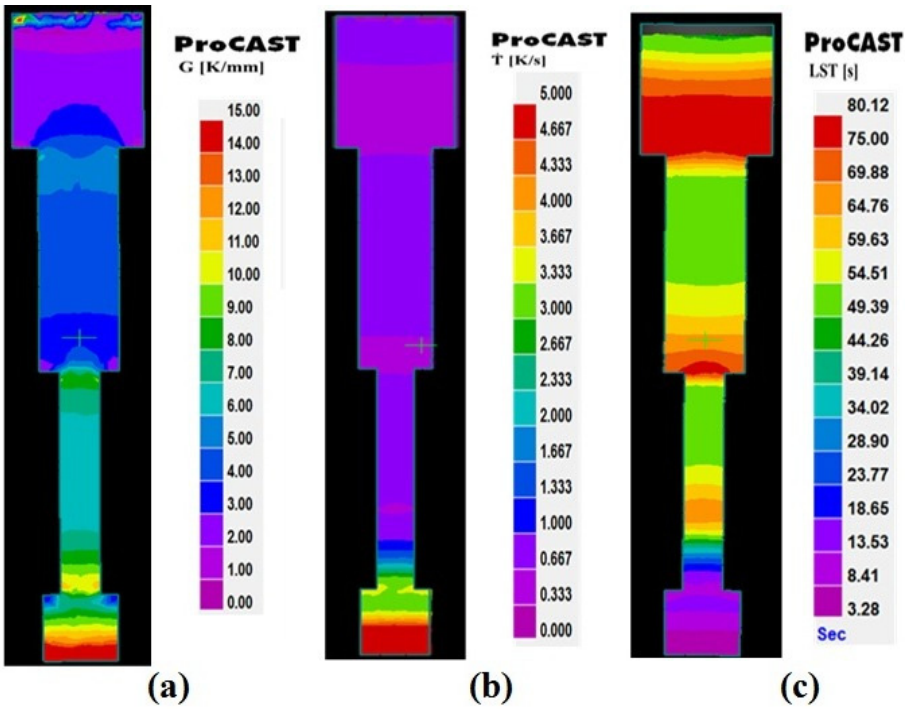

Fig. 9. Distribution of the simulated (a) temperature gradient, (b) cooling rate, and (c) local solidification time for the cylindrical specimen grown at 6 mm.min^{-1}.

9(b), respectively. It can be conceived that the formation of stray grains is due to the corresponding thermal condition in the platform region and the inclination angle of the liquidus isotherm which is in favour of nucleation and growth of new grains. These results clearly show that the platform size plays an important role, as it affects the corresponding thermal condition. No stray grain is formed in the platform L1 with the size of 4 mm, while several stray grains are formed in the L2 platform with the size of 5 mm, especially at the higher withdrawal rates. Distribution of the local solidification time is also shown in Fig. 9(c). As can be seen, the shortest solidification time is taken near the chill. The solidification time gradually increases by getting

far from the chill due to the decrease in temperature gradient. However, as the lateral heat transfer is increased with time, the solidification time is again decreased. The solidification time is then increased when passing the platform L1 followed by a decrease due to the lateral heat transfer.

3. 3. A Process Map for Stray Grain Formation

As already shown in Table 7, the formation of stray grain is promoted at a higher withdrawal velocity. In addition, more stray grains can be formed in a bigger platform. The initial size of the stepped specimen has also influence on the occurrence of stray grains. Considering all these parameters, the present simulation model was used to predict the formation of stray grains for different mould designs, in order to develop a suitable process map. As an example, the predicted number of stray grains in a cylindrical specimen with 8 mm initial diameter grown at different withdrawal velocities and platform designs is presented in Table 8. It can be seen that both withdrawal velocity and platform size have a direct influence on the stray grain formation. Figure 10 shows the predicted three-dimensional process map which relates all the influencing process parameters of withdrawal velocity, platform size and initial sample diameter on the number of stray grains in the stepped cylindrical specimens. This map presents a critical value for

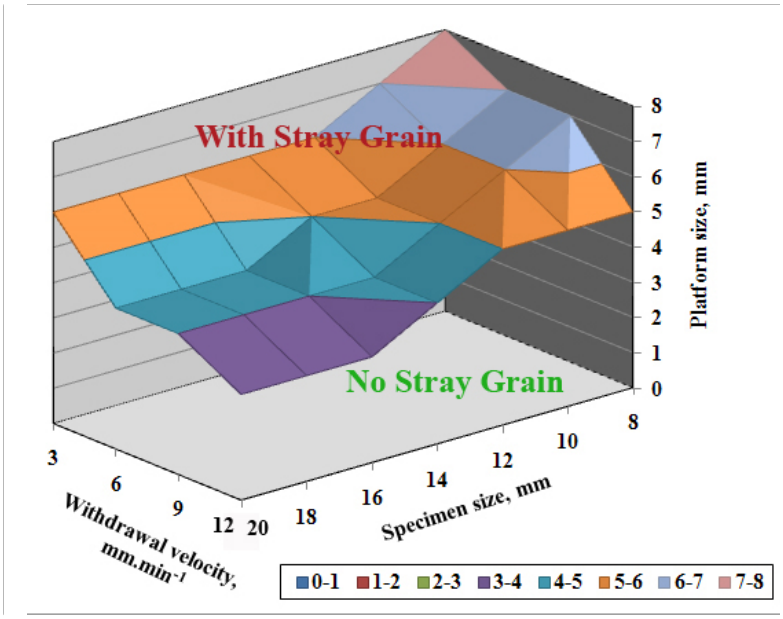

Fig.10. A process map for the formation of stray grain as functions of withdrawal velocity, platform size and initial specimen size for the directionally-solidified GTD-111 superalloy. This map shows the critical value (surface) of the process parameters for the formation of stray grains.

Table 7. Comparison of the experimental and simulated results for the number of stray grains in the L1 and L2 platforms of the cylindrical and cubic specimens directionally solidified at different withdrawal velocities of 3, 6, and 9 mm.min^{-1}.

Platform	Platform size, *d* (mm)	Initial sample diameter/side size, *D* (mm)	Cylindrical specimen						Cubic specimen					
			3 mm.min^{-1}		6 mm.min^{-1}		9 mm.min^{-1}		3 mm.min^{-1}		6 mm.min^{-1}		9 mm.min^{-1}	
			Sim	Exp	Sim	Exp	Sim	Exp	Sim	Exp	Sim	Exp	Sim	Exp
L1	4	8	0	0	0	0	0	0	0	0	1	1	2	2
L2	5	16	1	1	4	4	5	4	0	0	2	1	2	3

each process parameter to prevent the formation of stray grains. Increasing the withdrawal velocity decreases the critical platform size. As an example, for the initial diameter of 10 mm, no stray grain is formed at the velocity of 6 mm.min^{-1} in the platform of 6 mm, but for the platform of 7 mm, the velocity should be decreased to prevent the formation of stray grains. The process map is also shown that the critical platform size is reduced by increasing the initial sample diameter. As an example, for the platform size of 5 mm, if the initial diameter is 8 mm, no stray grain will be formed at the withdrawal velocity up to 10 mm.min^{-1}; however, if the initial diameter is increased to 16 mm, no stray grain region will be limited to the velocity of less than 4 mm.min^{-1}. All the experimental data reported in Table 7 would fit in the regions shown in Fig. 10. It should be added that the same procedure can be applied for the stepped cubic specimens, but the regions with different conditions may be determined for the stray grain formation in their process map. One practical way to prevent the formation of stray grains in the platform region of turbine blades is the application of a suitable withdrawal velocity regime based on the cross sectional area of the blade. A lower withdrawal velocity should be then used for a larger platform size or initial specimen size. Such a process map can be very suitable to predict the conditions for preventing the formation of stray grains based on different values of withdrawal velocity, platform size and initial sample size.

4. CONCLUSION

The formation of stray grain defects during directional solidification process of the GTD-111 Ni-based superalloy was investigated. Based on the application of the experimentally-validated simulation model, a process map for the formation of stray grains as functions of withdrawal velocity, platform size and initial sample size was presented. It was quantitatively shown how increasing the withdrawal velocity, the platform size and the initial specimen size favour the formation and growth of stray grains. The critical platform size to inhibit the formation of stray grains is not only depended on the withdrawal velocity, but also to the specimen size.

5. ACKNOWLEDGMENTS

The authors would like to thank the financial support of the project by Mapna Turbine Blade Engineering and Manufacturing Company and Mapna Group Research and Development department (Contract # B3029001-2).

REFERENCES

1. Reed, R. C., “The Superalloys Fundamentals and Applications, Cambridge, Cambridge University Press, 2006.
2. Zhou, Y., “Formation of stray grain during directional solidification of a nickel-based superalloy, Scripta Mater., 2011, 65, 281-284.
3. Imwinkelried, T., Desbiolles, J. L., Gandin, Ch-A., Rappaz, M., Rossmann, S., and Thévoz, Ph., “Modeling of Casting, Welding and Advanced Solidification Processes VI: The Minerals, Metals & Materials Society, 1993, 63-70.
4. Bussac, A. D., and Gandin, C. A. “Prediction of a process window for the investment casting of dendritic single crystals”, Mater. Sci. Eng. A, 1997, 237, 35-42.
5. Gu, J. P., Beckermann, Ch., and Giamei, A. F., “Motion and remelting of dendrite fragments during directional solidification of a Nickel-base superalloy”, Metall. Mater. Trans. A, 28A, 1997, 1533-1542.
6. D’Souza, N., Jennings, P.A., Yang, X.L., Lee, P D., McLean, M., Dong, H.B. 2005. Seeding of single-crystal superalloys—Role of constitutional undercooling and primary dendrite orientation on stray-grain nucleation and growth. Metall. Mater. Trans. B, 36, 657-666.
7. Ma, D., Bührig-Polaczek, A., “Development of heat conductor technique for single crystal components of superalloys”, Int. J. Cast Metals Res., 22, 2009, 422-429.
8. Xuan, W., Ren, Z., Li, C., Ren, W., and Chen, C., “Formation of stray grain in cross section area for Ni-based superalloy during directional solidification, The 3rd Int. Conf. on Advances in Solidification Processes, IOP Conf. Series, 27, 2011, 012035.

9. Yang, C., Liu, L., Zhao, X., Wang, N., Zhang, J., and Fu, H., "Competitive grain growth mechanism in three dimensions during directional solidification of a nickel-based superalloy", J. Alloys Comp., 2013, 578, 577-584.
10. Meng, X. B., Li, J. G., Chen, Z. Q., Wang, Y. H., Zhu, S. Z., Bai, X. F., Wang, F., Zhang, J., Jin, T., Sun, X. F. and Hu, Z. Q., "Effect of platform dimension on the dendrite growth and stray grain formation in a Ni-base single-crystal superalloy, Metall. Mater. Trans. A, 44A, 2013, 1955-1965.
11. Meng, X. B., Li, J. G., Zhu, S. Z., Du, H. Q., Yuan, Z. H., Wang, J. W., Jin, T., Sun, X. F., and Hu, Z. Q., "Method of stray grain inhibition in the platforms with different dimensions during directional solidification of a Ni-base superalloy", Metall. Mater. Trans. A, 2014, 45, 1230-1237.
12. D'Souza, N., Dong, H. B., Ardakani, M. G., Shollock, B.A., "Solidification path in the Ni-base superalloy, IN713LC—quantitative correlation of last stage solidification". Scripta Mater. 2005, 53, 729.
13. Long, F., Yoo, Y. S., Jo, C. Y., Seo, S. M., Jeong, H. W., Song, Y. S., Jina, T., Hu, Z. Q., "Phase transformation of and phases in an experimental nickel-based superalloy", J. Alloy. Comp., 2009, 478, 181–187.
14. ProCAST User's Manual, ESI Group, 2011.
15. Gandin, Ch-A., and Rappaz, M., "A coupled finite element-cellular automaton model for the prediction of dendritic grain structures in solidification process, Acta Metall. Mater., 42, 1994, 2233−2246.
16. Rappaz, M., "Modelling of microstructure formation in solidification processes, Int. Mater. Rev. 34(3), 1989, 93-123.
17. Szeliga, D., Kubiak, K., Burbelko, A., Motyka, M., Sieniawski, J., "Modeling of Directional Solidification of Columnar Grain Structure in CMSX-4 Nickel-Based Superalloy Castings, J. Mater. Eng. Perf. 23, 2014, 1088–1095.
18. Kurz, W., Giovanola, B., and Trivedi, T. R. "Theory of microstructural development during rapid solidification, Acta Metall., 1986, 34, 823.
19. Bobadilla, M., Lacaze, J. and Lesoult, G., "Influence des conditions de solidification sur le déroulement de la solidification des aciers inoxydables austénitiques, J. Cryst. Growth, 1998, 89, 531-544.
20. Kermanpur, A., Varahram, N., Davami, P. and Rappaz, M., "Thermal and grain-structure simulation in a land-based turbine blade directionally solidified with the liquid metal cooling process". Metall. Mater. Trans. B 31, 2000, 1293–1304.
21. Chalmers, B., "Principles of Solidification", John Wiley & Sons, New York, 1964.
22. Ding, G. L. and Tewari, S. N., "Dendritic morphologies of directionally solidified single crystals along different crystallographic orientations". J. Cryst. Grow. 2002, 236, 420–428.